Characterization of magnesium doped sol-gel biomaterial for bone tissue regeneration: the effect of Mg ion in protein adsorption

Authors

Andreia Cerqueira[1], Francisco Romero-Gavilán[1*], Iñaki García-Arnáez[2], Cristina Martinez-Ramos[3], Seda Ozturan[4], Raúl Izquierdo[1], Mikel Azkargorta[5], Félix Elortza[5], Mariló Gurruchaga[2], Julio Suay[1], Isabel Goñi[2]

[1]Department of Industrial Systems Engineering and Design, Universitat Jaume I, Av. Vicent Sos Baynat s/n, 12071 Castellón de la Plana, Spain

[2]Departament of Science and Technology of Polymers, Universidad del País Vasco, P. M. de Lardizábal, 3, 20018 San Sebastián, Spain

[3]Center for Biomaterials and Tissue Engineering, Universitat Politècnica de Valencia, Camino de Vera, s/n 46022 Valencia, Spain

[4]Department of Periodontology, Faculty of Dentistry, Istanbul Medeniyet University, Dumlupınar D100 Karayolu, 98, 34720 Istanbul, Turkey

[5]Proteomics Platform, CIC bioGUNE, Basque Research and Technology Alliance (BRTA), CIBERehd, ProteoRed-ISCIII, Bizkaia Science and Technology Park, 48160 Derio, Spain

*Corresponding author: Francisco Romero-Gavilán

Departamento de Ingeniería de Sistemas Industriales y Diseño, Campus del Ríu Sec, Avda. Vicent Sos Baynat s/n, 12071 – Castelló de la Plana (España)

E-mail: gavilan@uji.es

Abstract

Magnesium is the fourth most abundant element in the human body with a wide battery of functions in the maintenance of normal cell homeostasis. In the bone, this element incorporates in the hydroxyapatite structure and it takes part in mineral metabolism and regulates osteoclast functions. In this study, sol-gel materials with increasing concentrations of $MgCl_2$ (0.5, 1, and 1.5%) were synthesized and applied onto Ti surfaces as coatings. The materials were first physicochemically characterized. *In vitro* responses were examined using the MC3T3-E1 osteoblastic cells and RAW264.7 macrophages. Human serum protein adsorption was evaluated employing nLC-MS/MS. The incorporation of Mg did not affect the crosslinking of the sol-gel network, and a controlled release of Mg was observed; it was not cytotoxic at any of the tested concentrations. The cytoskeleton arrangement of MC3T3-E1 cells cultured on the Mg-doped materials changed in comparison with controls; the cells became more elongated, with protruded lamellipodia and increased cell surface. The expression of integrins (ITGA5 and ITGB1) was boosted by Mg-coatings. The ALP activity and expression of TGF-β, OSX and RUNX2 genes were also increased. In RAW264.7 cells, TNF-α secretion was reduced, while TGF-β and IL-4 expression rose. These changes correlated with the altered protein adsorption patterns. The Mg-doped coatings showed increased adsorption of anti-inflammatory (CLUS, IC1, CFAH, and VTNC), cell adhesion (DSG1, FILA2, and DESP) and tissue regeneration (VTNC and CYTA) proteins. This integrated approach to biomaterial characterization revealed the potential of Mg in bone tissue regeneration.

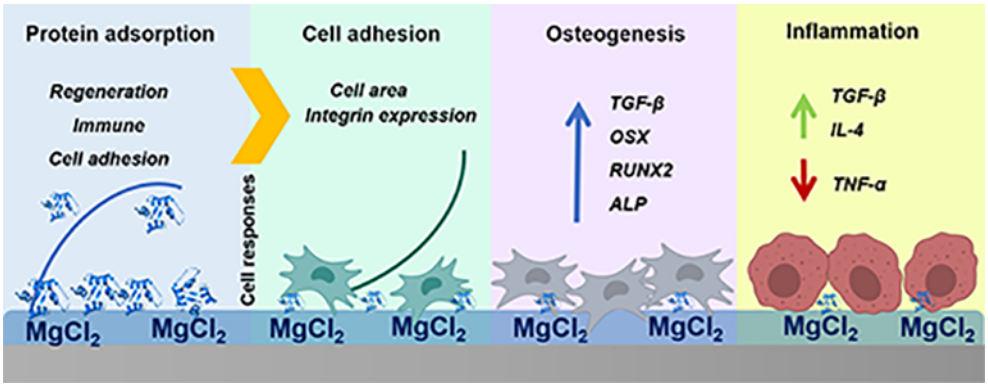

Keywords

Mg^{2+}, biomedical applications, osseointegration, proteomics, hybrids, integrins

1. Introduction

Magnesium (Mg) is the fourth most abundant element in the human body [1]. Approximately 60% of this element is stored in the bone as a part of the hydroxyapatite structure and takes part in the mineral metabolism [2,3]. Magnesium is involved in many normal cell functions, such as metabolic reactions and maintenance of cell membrane, DNA and protein structure. It is a key factor in the translation of genetic information and adenosine triphosphate (ATP) synthesis [3–5]. Magnesium deficiency has been associated with the promotion of osteoclastogenesis, which results in decreased bone formation and increased resorption [5]. Moreover, Mg modulates immune responses by regulating cytokine production [6] and the activation/suppression of the NF-κB signalling pathway [6,7]. The properties of Mg-based materials have been attracting increasing attention in the biomedical field. Bioactive glasses [8], biodegradable alloys (reviewed in [9]), bioglasses (reviewed in [10]) and Mg-enriched hydroxyapatites [11] have been studied, showing the potential of new Mg-based materials in bone repair and substitution [12,13].

Titanium (Ti) and its alloys are commonly employed in orthopedic implants used for bone and dental repair because of their attractive properties such as mechanical strength, excellent resistance to corrosion and biocompatibility [3]. The successful implementation of these materials depends on the capacity of host bone to establish intimate contact with the implant surface [14]. However, the relatively bioinert surface of Ti often causes implant failure and limits its clinical application [3]. Bioactive surface coatings, enhancing the osteoinductive properties of Ti materials, might present an interesting alternative.

The sol-gel technique can be employed to obtain metal surface coatings with a wide variety of advantages, such as improved control of the chemical composition of the coating and the film microstructure [15]. These coatings can also be used as controlled release vehicles [16]. Sol-gel precursors are easily available and mix at a molecular level, allowing the decrease of the sintering temperatures, making it a relatively inexpensive method [15]. Using 70% of methyltrimethoxysilane (MTMOS) and 30% of tetraethyl orthosilicate (TEOS) as precursors (MT), Martínez-Ibañez *et al.* [17] have obtained a sol-gel material with biomedical potential. It showed good osteointegration and osteogenic activity both *in vitro* and *in vivo* [18]. Thus, given the regenerative potential of magnesium, the development of a sol-gel coating capable of releasing Mg represents an interesting alternative to bioactivate titanium prostheses.

Biological response to an implanted device is determined by the conjugation factors. The initial processes are crucial. They determine a material outcome *in vivo*, and the provisional matrix formed by blood proteins adsorbed onto a surface upon implantation defines the consequent cellular and tissular responses [19]. This protein adsorption depends on the material surface properties, such as wettability, roughness and charge [20].

New sol-gel coatings doped with increasing percentages of Mg (0.5%, 1% and 1.5%) were synthetized to be applied to a Ti surface. We synthesized the coatings and characterized its physicochemical properties and

examined *in vitro* cell responses using the MC3T3-E1 osteoblasts and RAW264.7 macrophages. Human serum protein adsorption onto the material surface was analyzed employing the nLC-MS. With this results, we aim to give a broad insight and improve the understanding of the potential of Mg ion in biomedical applications.

2. Materials and methods

2.1. Sol-gel synthesis and sample preparation

To obtain the hybrid coatings with different percentages of $MgCl_2$ (**Table 1**), the sol-gel route was employed, using MTMOS and TEOS precursors in a molar ratio of 7:3. The alkoxysilanes were dissolved in 2-propanol (50 % v/v). The corresponding stoichiometric amount of 0.1N HNO_3 (to hydrolyze the precursors completely), and the appropriate amounts of $MgCl_2$ were added to the mix at a rate of 1-drop s^{-1}. All the reagents were purchased from Merck (Darmstadt, Germany). The sol-gel mixtures were kept under stirring for 1 h and then 1 h at rest. Sandblasted, acid-etched (Romero-Gavilán *et al.* [21]) grade-4 Ti discs (12-mm diameter, 1-mm thick) were used as a substrate for the coatings. The sol-gels were applied with a dip-coater (KSV DC; KSV NIMA, Espoo, Finland). The discs were immersed in the sol-gel solutions at a speed of 60 cm min^{-1}, kept submerged for one minute, and removed at a 100 cm min^{-1}. Glass-slides were employed as a substrate to prepare samples for hydrolytic degradation and Mg^{2+} release assays. The slides were pre-treated with HNO_3 solution (25 % v/v) in an ultrasonic bath (Sonoplus HD 3200; Bandelin Electronic, Berlin, Germany) for 20 min at 30 W. Next, they were washed in the ultrasonic bath with distilled water and dried at 100 °C. This pre-treatment aimed to clean the glass surfaces and ensure the material-glass adhesion. At this point, the glass substrates were coated by casting. The coating adherence and thickness was measured applying the sol-gel formulations onto AISI 316-L stainless steel plates (5 cm x 5 cm; RNSinox S.L., Spain). The stainless-steel surfaces were pre-treated by polishing and cleaned with acetone to remove impurities. The coatings were applied onto the stainless steel by dip-coating in the same conditions as Ti discs. For thickness measurements, adhesive tape was applied to the substrate covering a part of it. After dip-coating, the tape was removed creating a border that allows the thickness measurement of the deposited sol-gel film. For chemical characterization, free films of the synthesized sol-gel compositions were obtained by pouring the 5 mL of each solution into non-stick Teflon molds. Finally, to cure the sol-gel, all the samples were subjected to heat treatment, at 80 °C for 2 h.

Table 1. Nomenclature of the sol-gel networks with different amounts of $MgCl_2$. The mass percentages are relative to the total amount of alkoxysilane.

Nomenclature	Sol-gel network	$MgCl_2$ (wt%)
MT	70M30T	0
MT0.5Mg	70M30T	0.5
MT1Mg	70M30T	1
MT1.5Mg	70M30T	1.5

2.2. Physicochemical characterization

A Thermo Nicolet 6700 Fourier-transform infrared spectrometer (FT-IR; Thermo Fisher Scientific, NY, US) with an attenuated total reflection system (ATR) was employed to characterize the sol-gel networks. The spectra were measured in the 4000–400 cm^{-1} wavenumber range. In parallel, the solid-state ^{29}silicon nuclear magnetic resonance spectroscopy (^{29}Si-NMR) technique was used to study the reticulation level of the synthesized structures. To this purpose, we employed a Bruker 400 AVANCE III WB Plus spectrometer (Bruker, Billerica, MA, US) with a cross-polarization magic-angle spinning (CP-MAS) probe for solid samples. The pulse sequence was the Bruker standard: 79.5-MHz frequency, 5-kHz spectral width, 2-ms contact time and 5-s delay time. The spinning speed was 7.0 kHz. X-ray diffraction analysis (XRD) was carried out to study the crystalline or amorphous nature of the synthetized materials with a Bruker D4-Endeavor diffractometer (Bruker). Measurements in the range of 5–70° (2θ) with a step size of 0.02°(2θ) and a scanning rate 4 s $step^{-1}$ were collected with filtered CuKα radiation (λ = 1.54 A), an operating voltage of 40 kV and a filament current of 40 mA. In addition to analyzing the different formulations, with and without magnesium, an $MgCl_2$ sample was analyzed as a control.

The coating attachment was analyzed, evaluated and classified by the cross-cut test following the UNE EN-ISO 2409 norm. A mechanical profilometer Dektack 6 (Veeco; Munich, Germany) was employed to measure the thickness of the coating applied onto the stainless steel plates. Profiles from the uncoated area to the coated area were taken, measuring the rise between coated and uncoated areas. Three individual samples were analyzed, performing three measurements in each of them.

A scanning electron microscope (SEM; Leica-Zeiss LEO, Leica, Wetzlar, Germany) was used to examine the coating morphologies onto Ti discs. Platinum sputtering was employed to increase the sample conductivity. An optical profilometer PLm2300 (Sensofar, Barcelona, Spain) was used to characterize the sample roughness. Three samples of each material were evaluated, and three measurements were carried out for each sample to obtain an average value of Ra (arithmetic average roughness parameter) for each surface. An automatic contact angle meter OCA 20 (DataPhysics Instruments, Filderstadt, Germany) was employed to characterize the surface wettability of the coated Ti surfaces. Ultrapure water drops of 10 µL were deposited on the material at a speed of 27.5 µL s^{-1}. The drop images were examined using SCA 20 software (DataPhysics Instruments). Six samples of each type were tested, depositing two drops on each disc.

The mass loss during sample incubation in 50 mL of distilled water at 37 °C was recorded to examine the rate of hydrolytic degradation. Samples were removed after 7, 14, 28, 42, and 56 days of incubation. The results were calculated as a percentage (%) of the initial mass lost. Three independent samples were evaluated for each condition. The amount of Mg^{2+} released from the coatings was measured using an inductively coupled

plasma mass spectrometer (Agilent 7700 Series ICPMS; Agilent Technologies, Santa Clara, CA, US). The materials were incubated in ddH_2O at 37 °C for 28 days. Aliquots of 0.5 mL were removed after 2, 4, 6, 8, 24, 72, 168, 336, 504 and 672 h of incubation. Each data point is the average of the values obtained for three replicas.

2.3. In vitro assays

2.3.1. Cell culture

Mouse calvaria osteosarcoma (MC3T3-E1) cell line was seeded onto the materials in low-glucose DMEM (Gibco, Life Technologies, Thermo Fisher Scientific) with 1 % penicillin/streptomycin (Gibco) and 10 % foetal bovine serum (FBS; Gibco). After 24 h, the cell culture medium was replaced with osteogenic medium (DMEM, 1 % penicillin/streptomycin, 10 % FBS, 1 % ascorbic acid (5 $\mu g\ mL^{-1}$), and 100 mM β-glycerol phosphate), which was changed every two days. Mouse murine macrophage (RAW264.7) cell line was cultured in high-glucose DMEM supplemented with 1 % penicillin/streptomycin and 10 % FBS. Cell culture was carried out in a humidified (95 %) incubator at 37 °C, with 5 % CO_2.

2.3.2. Cytoskeleton arrangement

For the evaluation of cytoskeleton arrangement, MC3T3-E1 cells were seeded on the materials at a density of 1×10^4 cells cm^{-2} for 1 day. Then, the samples were washed once with PBS, fixed with 4 % paraformaldehyde (PFA) for 20 min at room temperature and permeabilized with 0.1 % Triton X-100 for 5 min. Next, the samples were incubated with phalloidin (1:100; Abcam, Cambridge, UK) diluted in 0.1 % w/v bovine serum albumin (BSA)-PBS for 1 h at room temperature. For nuclei staining, after washing twice with PBS, the samples were incubated for 5 min in a mounting medium with DAPI (Abcam). A Leica TCS SP8 Confocal Laser Scanning Microscope with 20x (dry) lenses was employed for fluorescence detection. The images were obtained using LAS X software (Leica) and analyzed using Image J software (National Institutes of Health, Maryland, USA).

2.3.3. Cytotoxicity and ALP activity

Biomaterial cytotoxicity was assessed using the MC3T3-E1 cells, following the ISO 10993-5:2009 (Annex C) [22] standards, and samples were prepared according to the ISO 10993-12:2012 [23]. The CellTiter 96® Proliferation Assay (MTS; Promega, Madison, WI), based on the formazan formation, was used according to manufacturer's guidelines. For controls, cells incubated without (negative control) and with latex (positive control) were used. The material was considered cytotoxic when the cell viability fell below 70 %.

To evaluate the effects on cell mineralization, the MC3T3-E1 cells were cultured on the materials at a density of 1.75×10^4 cells cm^{-2} for 7 and 14 days. At each time point, alkaline phosphatase activity (ALP) activity was

measured following the protocol of Araújo-Gomes *et al.* [18] and normalized to protein content obtained using a Pierce BCA assay kit (Thermo Fisher Scientific).

2.3.4. Cytokine quantification using ELISA

For measuring the levels of secreted cytokines, the cell culture medium used to incubate the RAW264.7 cell-seeded discs was collected and frozen until further analysis. The concentrations of tumor necrosis factor (TNF)-α and transforming growth factor (TGF)-β were determined using an ELISA (Invitrogen, Thermo Fisher Scientific) kit, according to the manufacturer's instructions.

2.3.5. Relative gene expression: RNA extraction, cDNA synthesis and qRT-PCR

To examine the effects of the Mg-doped materials on gene expression, the MC3T3-E1 cell line was cultured at a density of 1.75 x 10^4 cells cm^{-2} for 7 and 14 days and RAW264.7 at a density of 30 x 10^4 cells cm^{-2} for 2 and 4 days. Total RNA was extracted with TRIzol as described in Cerqueira *et al.* [24]. RNA concentration, integrity, and quality were measured using NanoVue® Plus Spectrophotometer (GE Healthcare Life Sciences, Little Chalfont, UK). For cDNA synthesis, approximately 1 µg of total RNA was converted into cDNA using PrimeScript RT Reagent Kit (Perfect Real Time; TAKARA Bio Inc., Shiga, Japan). The reaction was carried out in a Prime Thermal Cycler (Techne, Staffordshire, UK) as described in Cerqueira *et al.* [24]. The resulting cDNA was diluted in DNase-free water to a concentration suitable for gene expression evaluation.

Quantitative real-time PCRs (qRT-PCR) were carried out in 96-well plates (Applied Biosystems®, Thermo Fisher Scientific). Each sample represented the gene of interest and the housekeeping gene (*GAPDH*). Primers for each gene were designed (using Primer3Plus software tool) from specific DNA sequences obtained from NCBI and purchased from Thermo Fisher Scientific. The targets studied for each cell line are shown in **Supplementary Table 1**. Reactions were carried out as described in Cerqueira *et al.* [24] in a StepOne Plus™ Real-Time PCR System (Applied Biosystems®). Fold changes were calculated using the $2^{-\Delta\Delta Ct}$ method, and data were normalized to blank wells (without materials).

2.4. Adsorbed protein layer and proteomic analysis

To obtain the proteins adsorbed onto the material surface, samples were incubated for 3 h (37 °C, 5 % CO_2) in 24-well NUNC plates (Thermo Fisher Scientific) with 1 mL of human serum from male AB plasma (Merck). The materials were washed five times with ddH_2O and once with wash buffer (100 mM NaCl, 50 mM Tris–HCl, pH 7.0) to eliminate non-adsorbed proteins. Adsorbed proteins were obtained by elution (0.5 M triethylammonium bicarbonate buffer (TEAB), 4 % sodium dodecyl sulfate (SDS), 100 mM dithiothreitol (DTT); Merck). For each surface, four independent replicates were analyzed, and each replicate was a pool of eluate from four discs. Total serum protein concentration was determined using a Pierce BCA assay kit (Thermo Fisher Scientific).

For proteomic analysis, the eluate was characterized employing electrospray tandem mass spectrometry, using a nanoACQUITY UPLC (Waters, Milford, MA) coupled to an Orbitrap XL (Thermo Electron, Bremen, Germany), following the protocol described in Romero-Gavilán *et al.* [25]. Each sample was analyzed in quadruplicate. Proteomic results were examined using PEAKS (Bioinformatics Solutions Inc., Waterloo, Canada), and the functional classification of the identified proteins was performed employing PANTHER software (http://www.pantherdb.org/).

2.5. Statistical analysis

Physicochemical and *in vitro* assay data were analyzed via one-way analysis of variance (ANOVA) with Tukey post hoc test, after confirming normal distribution and equal variance. Statistical analysis was performed using GraphPad Prism 5.04 software (GraphPad Software Inc., La Jolla, CA). The differences between MT and Mg-doped MT were considered statistically significant at $p \leq 0.05$ (*), $p \leq 0.01$ (**), and $p \leq 0.001$ (***). Data were expressed as means ± standard error (SE).

In the proteomic analysis, a Student's *t*-test was conducted to evaluate differences between MT and MT with different Mg concentrations, using Progenesis software. Differences were considered statistically significant at $p \leq 0.05$ and the ratio difference bigger than 1.3 in either direction (higher or lower).

3. Results

3.1. Physicochemical characterization

Hybrid sol-gel networks containing different amounts of $MgCl_2$ were synthesized using the sol-gel route. The effect of this compound on the sol-gel structure was studied using FT-IR, ^{29}Si-NMR and XRD (**Figure 1**). The FT-IR spectra demonstrated the presence of MTMOS-associated organic groups in the final networks; the bands corresponding to Si-C and C-H bonds were detected at 1270 and 2980 cm^{-1} [26], respectively. The signals seen at 760, 1020 and 1120 cm^{-1} were related to the formation of Si-O-Si bonds, and the band at 950 cm^{-1} indicated the presence of non-condensed Si-OH species [21]. These results are confirmed by the ^{29}Si-NMR spectra, which can verify the proper formation of the polysiloxane network (**Figure 1b**). Signals associated with the MTMOS trifunctional alkoxysilane (T units) are detected between -50 and -70 ppm. Within this range, the peaks at -57 and -66 ppm indicate the presence of T^2 and T^3 species [26], respectively. The TEOS tetrafunctional (Q units) chemical shifts are in the range between -97.5 and -115 ppm; the signals at -102 and -110 ppm reflect the presence of Q^3 and Q^4 species, respectively [27]. A good degree of crosslinking was achieved in the materials synthesized here; only the species with the highest degree of condensation were detected in the sol-gel structure. Moreover, it seems that the $MgCl_2$ incorporation into the sol-gel did not affect the final silica network crosslinking as all the spectrum shapes were similar. **Figure 1c** shows the XRD spectra obtained for the different sol-gel materials and for the $MgCl_2$. The obtained patterns for all the sol-gel formulations doped with $MgCl_2$ can be associated with an amorphous nature as no peaks related to $MgCl_2$ or other crystalline

structures were detected. In addition, no significant differences were found between the distinct Mg-doped compositions and MT. The broad and undefined peak around 10° (2θ) in the sol-gel material spectra can be associated with the presence of not completely hydrolyzed precursors. Another peak with similar shaped but less intensity was detected around 21° (2θ), being this signal characteristic of the SiO_2 amorphous sol-gel structures [28].

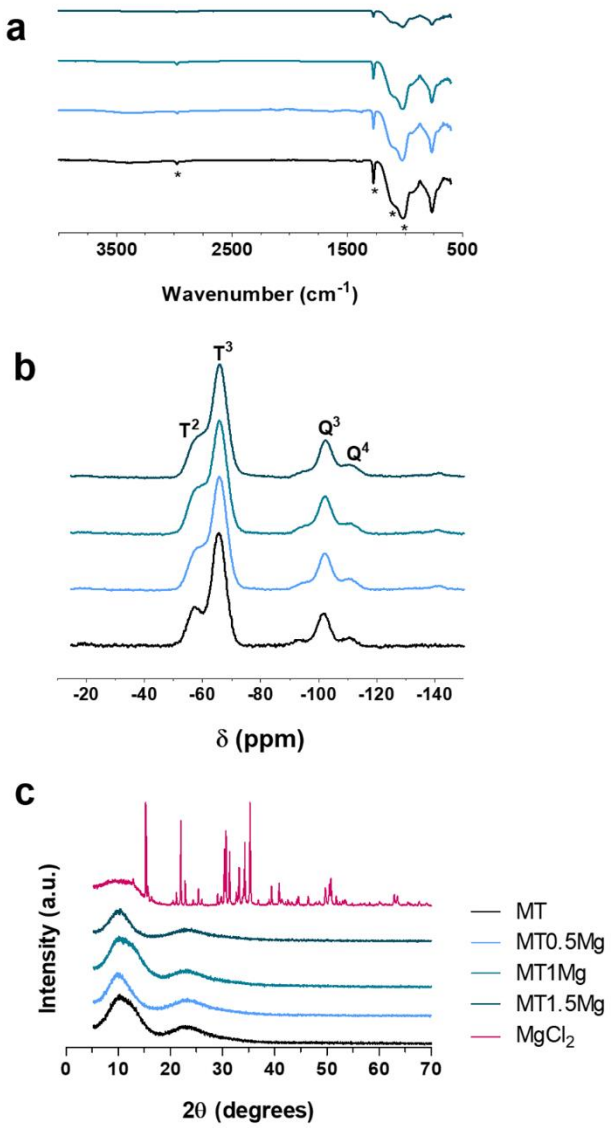

Figure 1: (a) FT-IR, (b) ^{29}Si-NMR and (c) XRD spectra of the studied sol-gel networks.

All sol-gel materials coatings showed a high degree of adherence (Class 0) based on the cross-cut test, as the edges of the cuts were smooth, and detachments were not observed (**Supplementary Figure 1a**). The coatings applied onto Ti were morphologically evaluated by SEM. The micrographs show that the different

compositions covered the whole area of Ti substrates (**Figure 2a-e**). Nevertheless, the sol-gel seemed to accumulate in the cavities associated with the Ti roughness, smoothing the initial morphological irregularities of the Ti surface. No $MgCl_2$ precipitates were detected. However, small holes of around 0.2–0.3 µm in diameter can be seen in the film with the largest amount of $MgCl_2$ (MT1.5Mg); these are not observed in other compositions (**Figure 2f**). The materials with $MgCl_2$ have the Ra roughness values similar to the Ra of the coating without Mg salt (**Figure 2g**). Additionally, the thickness measurements for the different coatings showed that the obtained sol-gel films do not have differences in thickness regardless of the amount of $MgCl_2$ added (**Supplementary Figure 1b**). The wettability results showed higher contact angles for materials with Mg than for the MT base material (**Figure 2h**). The coatings with $MgCl_2$ were more hydrophobic than MT, reaching the values of around 80° (close to those for uncoated Ti).

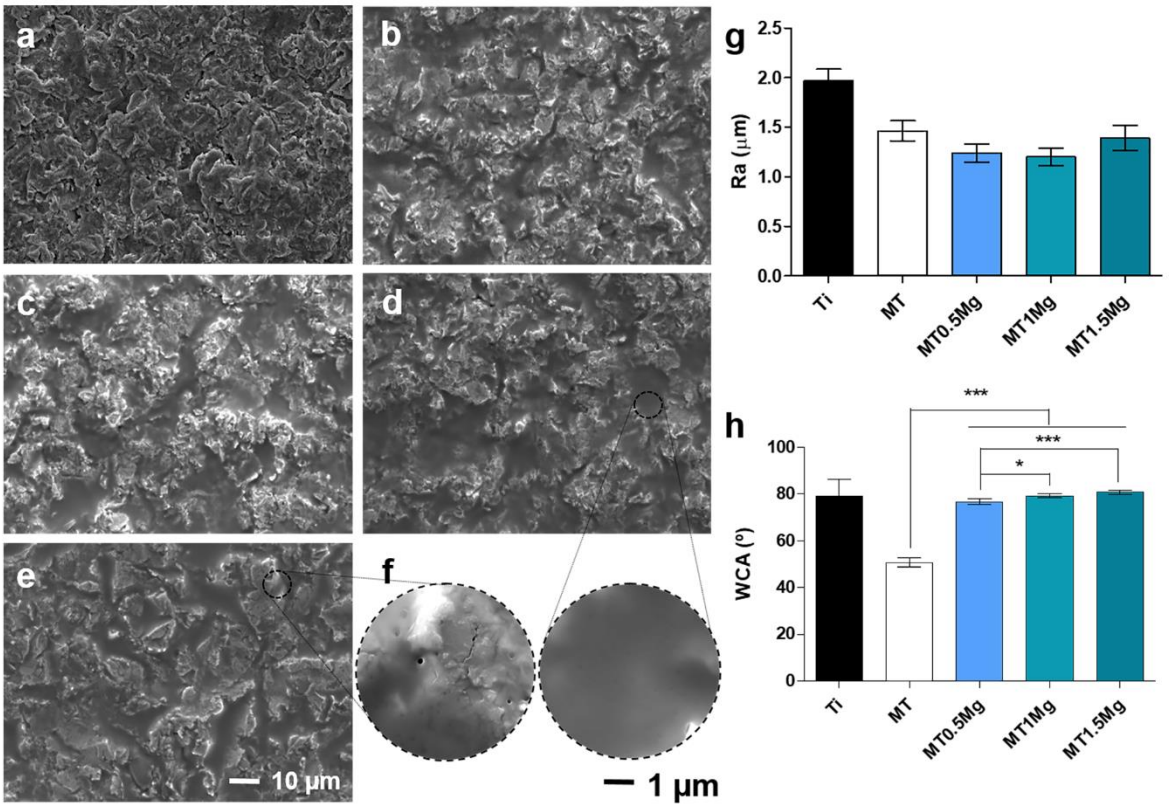

Figure 2: SEM microphotographs of (a) Ti, (b) MT, (c) MT0.5Mg, (d) MT1Mg, (e) MT1.5Mg and (f) enlarged areas of MT1Mg and MT1.5Mg coatings. Scale bars: (a-e) 10 and (f) 1 µm. Roughness Ra (g) and contact angle (WCA; h) are also displayed. Results are shown as means ± SE. The asterisks ($p \leq 0.05$ (*) and $p \leq 0.001$ (***)) indicate significant differences between MT and Mg-doped MT.

The Mg-containing coatings had a higher degradation rate than the base coating MT (**Figure 3a**). The base network showed a mass loss of around 18 % after 56 days of incubation. This mass loss increased as more $MgCl_2$ was incorporated into the sol-gel, reaching a value of around 28 % for the MT1.5Mg coating. The

amount of Mg^{2+} ions released also rose with the increasing salt content in the sol-gel compositions (**Figure 3b**). Moreover, the Mg^{2+} liberation process continued throughout the studied period (28 days).

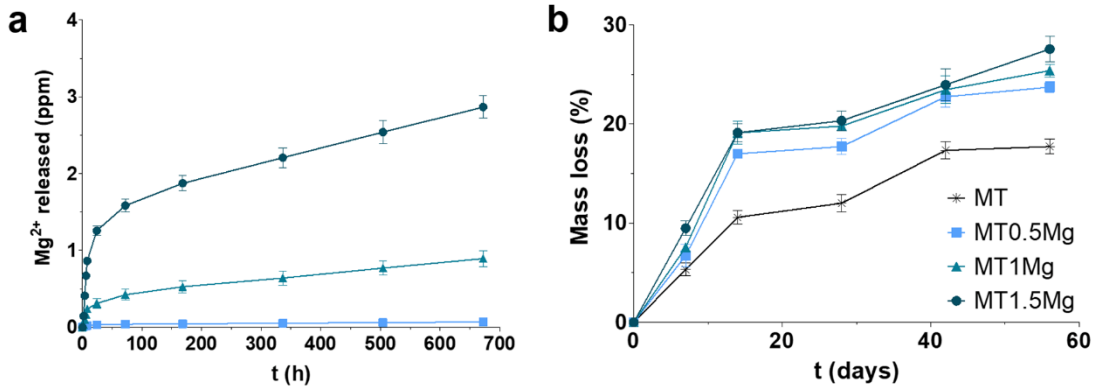

Figure 3: Release kinetics of Mg^{2+} ions (a) and hydrolytic degradation (b) of the sol-gel coatings enriched with $MgCl_2$. Bars indicate standard errors.

3.2. In vitro assays

3.1.1. Cytoskeleton arrangement, cytotoxicity and ALP activity

To examine the arrangement of cellular cytoskeleton, the cells were stained with phalloidin after 1 day of culture (**Figure 4 a-e**). The cells cultured on Ti and MT showed a triangular shape with few lamellipodia, while cells on the materials with Mg displayed a more elongated with protruding lamellipodia (white arrows). The MC3T3-E1 cells cultured on MT1Mg and MT1.5Mg also displayed protruding filopodia. Cells growing on MT1Mg and MT1.5Mg materials had significantly larger surface area than those cultured on the MT discs (**Figure 4f**).

None of the materials in the study was cytotoxic (data not shown). ALP activity showed a small decrease for MT0.5Mg and MT1Mg at 7 and 14 days, and a significant activity increase at 7 and 14 days for MT1.5Mg (**Figure 4g**).

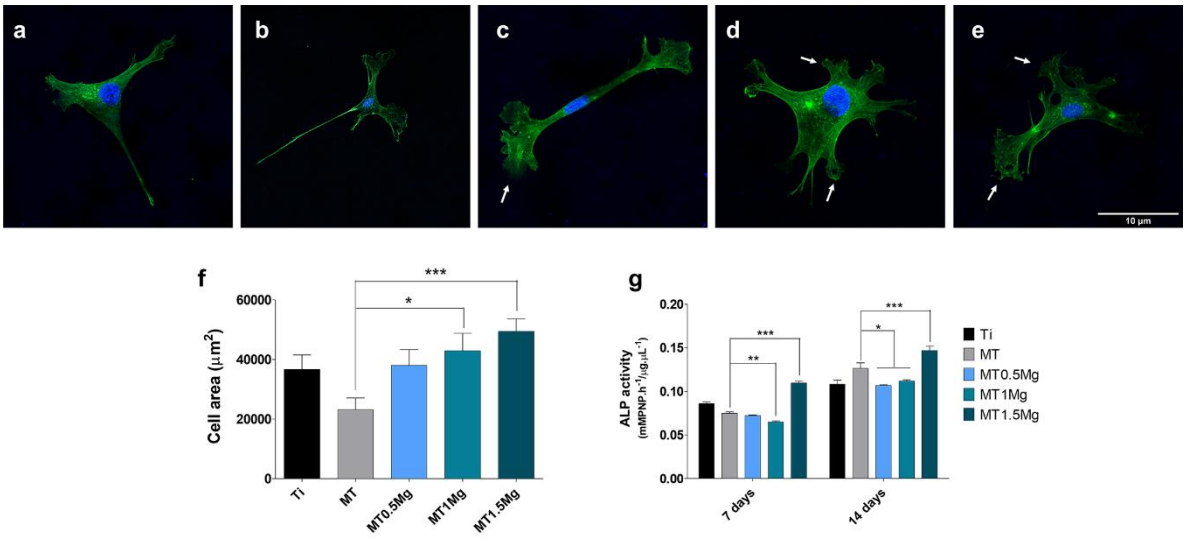

287

288 **Figure 4:** Fluorescent confocal images of cytoskeleton arrangement of MC3T3-E1 on (a) Ti, (b) MT, (c)
289 MT0.5Mg, (d) MT1Mg and (e) MT1.5Mg and (f) area of the cells adhered to the materials (f). Actin filaments
290 were stained with phalloidin (green), and nuclei were stained with DAPI (blue). Scale bar: 10 µm. ALP activity
291 (g) of MC3T3-E1 cells at 7 and 14 days. Results are shown as means ± SE. The asterisks ($p \leq 0.05$ (*), $p \leq 0.01$
292 (**), and $p \leq 0.001$ (***)) indicate statistically significant differences between MT and Mg-doped MT.

293 ### 3.1.2. Cytokine secretion measurements by ELISA

294 To evaluate the effect of Mg-doped materials on inflammation, cytokine secretion to the RAW264.7 cell
295 culture medium was examined. The levels of anti-inflammatory cytokine TGF-β increased significantly only in
296 cultures on MT1.5Mg, at 4 days (**Figure 5a**). In contrast, after 2 days, the amounts of secreted pro-
297 inflammatory cytokine TNF-α significantly decreased for all materials (**Figure 5b**). After 4 days, the TNF-α
298 excretion levels were similar for all the materials, with a significant decrease for MT1Mg in comparison with
299 MT.

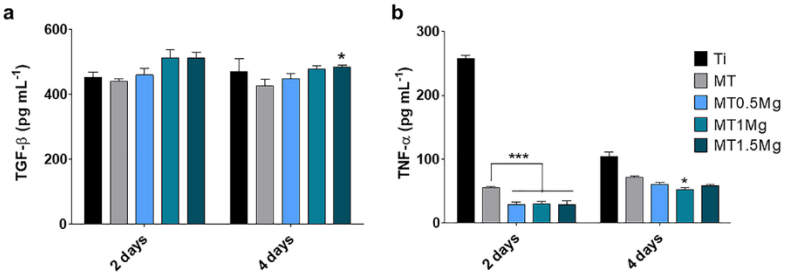

300

301 **Figure 5:** ELISA results for (a) TGF-β and (b) TNF-α for RAW264.7 cultures at 2 and 4 days. Data are shown as
302 means ± SE. The asterisks ($p \leq 0.05$ (*) and $p \leq 0.001$ (***)) indicate statistically significant differences between
303 MT and Mg-doped MT.

3.1.3. Relative gene expression

To further understand the effects of the Mg-doped materials on osteogenesis (ALP, TGF-β, OSX, and RUNX2), cell adhesion (ITGA5 and ITGB1), and inflammatory responses (IL-6, TNF-α, TGF-β, and IL-4), gene expression of selected targets was measured. In the case of osteogenic markers, after 7 days of culture, the ALP expression was similar for all materials. However, there was a significant increase in its expression on MT0.5Mg at 14 days (**Figure 6a**). The TGF-β expression was increased in MT0.5Mg and MT1.5Mg after 7 days. After 14 days, it was significantly augmented in MT0.5Mg and MT1Mg cultures and decreased on MT1.5Mg materials (**Figure 6b**). The expression of OSX showed a significant increase for all Mg-doped materials at both time points (**Figure 6c**). The expression of RUNX2 was only augmented for MT1.5Mg at 7 days. After 14 days, it increased significantly in the MT1Mg cultures and decreased for MT1.5Mg (**Figure 6d**). In the case of cell adhesion markers, ITGA5 expression rose for MT0.5Mg at 7 days and for MT1Mg and MT1.5Mg at 14 days (**Figure 6e**). The expression of ITGB1 increased for MT1.5Mg at 7 days, and for MT1Mg at 14 days (**Figure 6f**).

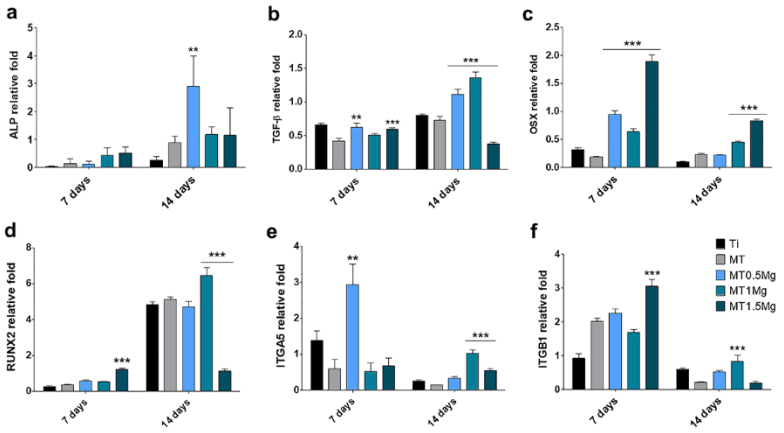

Figure 6: Gene expression of (a) alkaline phosphatase (ALP), (b) transforming growth factor (TGF-β), (c) osterix (OSX), (d) runt-related transcription factor 2 (RUNX2), (e) α5-integrin (ITGA5), and (f) β1-integrin (ITGB1) in MC3T3-E1 cultures at 7 and 14 days. Gene expression was normalized to blank wells (without any material) using the $2^{-\Delta\Delta Ct}$ method. Results are shown as means ± SE. The asterisks ($p \leq 0.05$ (*), $p \leq 0.01$ (**), and $p \leq 0.001$ (***)) indicate statistically significant differences between MT and Mg-doped MT.

Among the genes related to macrophages responses, the expression of pro-inflammatory marker IL-6 was significantly altered only in MT1.5Mg cultures at 4 days (**Figure 7a**), while TNF-α expression increased for MT1Mg and MT1.5Mg at 2 days (**Figure 7b**). The expression of anti-inflammatory marker TGF-β (**Figure 7c**) increased on MT1Mg and MT1.5Mg at 2 days. All the materials showed an increase in its expression at 4 days. The expression of IL-4 was rose for MT0.5Mg at 2 days and for MT1Mg, at 4 days (**Figure 7d**).

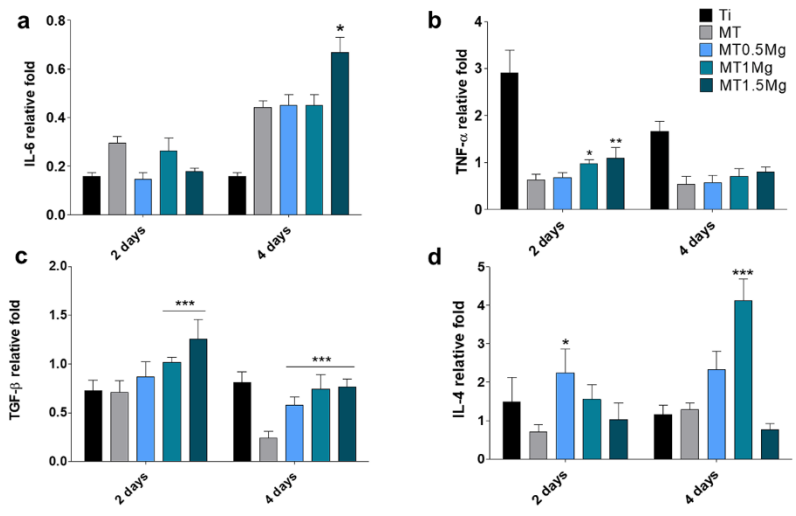

Figure 7: Gene expression of (a) interleukin (IL)-6, (b) tumor necrosis factor (TNF)-α, (c) transforming growth factor (TGF)-β, and (d) IL-4 in RAW264.7 macrophages after 2 and 4 days of culture. Gene expression was normalized to blank wells (without any material) using the $2^{-\Delta\Delta Ct}$ method. Results are shown as means ± SE. The asterisks ($p \leq 0.05$ (*), $p \leq 0.01$ (**), and $p \leq 0.001$ (***)) indicate statistically significant differences between MT and Mg-doped MT.

3.3. Proteomic analysis

The nLC-MS/MS analysis of eluted proteins identified 22 proteins preferentially adsorbed on the materials with Mg in comparison with the MT base material (**Supplementary Table 2**; **Table 2**). Among these, six proteins are related to complement system activation (CO9, CO3 and C1QC) and its inhibition (IC1, CLUS, and CFAH). Some other proteins associated with immune responses were also more abundant on the Mg-doped coatings. A1AT, which regulates the activity of neutrophil granulocytes, two immunoglobulins (LAC3 and IGHM) and a pentraxin (SAMP) were more absorbed. Three cell adhesion proteins preferentially attached to the materials containing Mg (DSG1, FILA2 and DESP). Similarly, VTNC and CYTA, which present a battery of functions related to tissue regeneration, regulation/inhibition of immune responses and cell attachment, preferentially adhered to Mg-doped MT. Moreover, several apolipoproteins related to lipid metabolism (APO2, APOA1, APOA4 and APOL1) were identified as well as two proteins associated with coagulation (SPB12 and A2MG) and one associated with DNA damage repair (UBB).

PANTHER analysis was used to associate the differentially adsorbed proteins with their biological functions and pathways. **Figure 6** shows pie-chart diagrams of the biological functions and pathways for the proteins differentially adsorbed onto the Mg-doped surfaces in comparison with MT. Among the various biological functions found, the immune system, cellular organization and process, multi-organism and multicellular organismal process, biological regulation, developmental and metabolic process and biological adhesion were

identified for all materials with Mg. For MT1Mg and MT1.5Mg, signaling and biological functions also appeared. The search for pathway associations revealed blood coagulation pathway for proteins from MT0.5Mg and MT1Mg materials. For the MT1Mg material, CCKR signaling map and B cell activation were also identified. For MT1.5Mg, only the CCKR signaling map pathway appeared.

Table 2. Ratios of different proteins differentially adsorbed onto the sol-gel materials doped with Mg, associated with relevant biological processes (immune response, cell adhesion, tissue regeneration and coagulation).

		Ratio		
Protein	**Biological process**	**MT0.5Mg/MT**	**MT1Mg/MT**	**MT1.5Mg/MT**
CO9	Immune responses	2.13	16.17	11.05
SAMP		6.97	12.77	9.63
CLUS		6.20	8.07	7.36
CFAH		3.63	5.51	5.34
A1AT		4.04	3.96	4.16
LAC3		1.00	6.54	3.69
IC1		2.91	3.47	3.56
C1QC		2.25	3.14	3.31
CO3		1.51	1.79	1.86
IGHM		1.37	2.17	1.84
APOA2		1.66	17.26	10.16
APOA1		1.18	2.73	3.52
APOA4		1.68	3.97	2.42
APOL1		1.18	4.50	2.32
CYTA	Tissue regeneration	2.24	10.68	10.89
VTNC		2.07	3.28	3.86
DSG1	Cell adhesion	11.36	19.75	10.57
FILA2		3.18	39.49	5.21
DESP		6.07	3.78	1.90
SPB12	Coagulation	1.50	6.05	4.00
A2MG		5.29	5.11	2.13

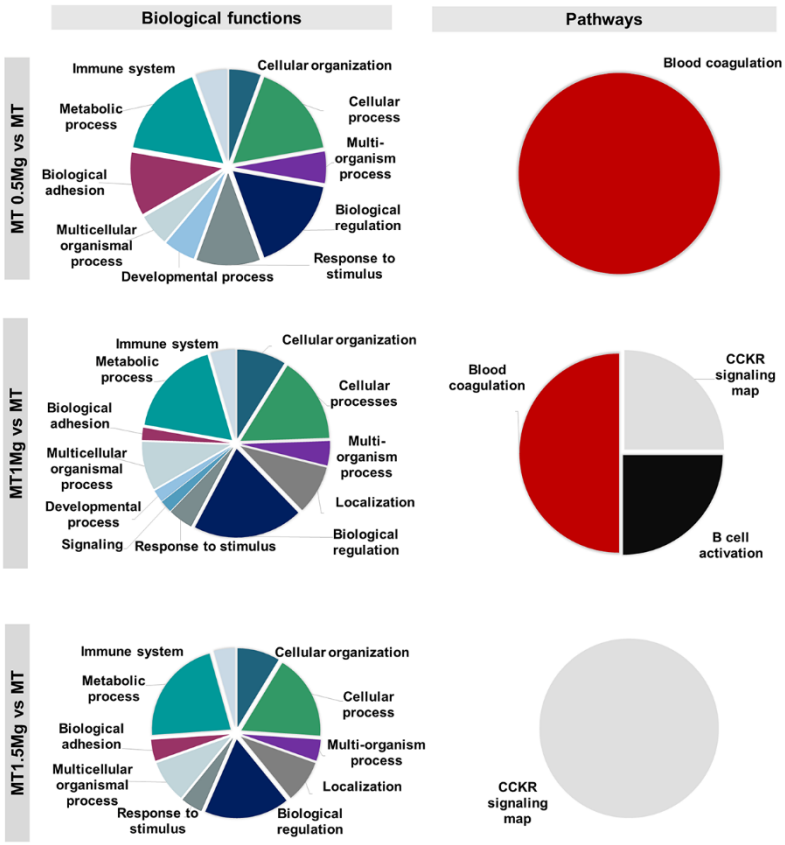

Figure 8: PANTHER diagram of biological functions and pathways associated with the proteins differentially adhering to Mg-enriched coatings in comparison with MT (without Mg).

4. Discussion

For a successful bone substitution, a material should have high mechanical strength and good biocompatibility and bioactivity [29]. Titanium and its alloys used to manufacture implants and have a wide application. However, from a biological standpoint, this type of material is relatively bioinert. A promising research line in the development materials is creating bioactive coatings capable of enhancing the tissue regeneration responses [3]. Sol-gels have been already used as coatings for Ti surfaces as they can release ions and other molecules in a controlled manner [24,30,31]. Magnesium is an important ion involved in a wide range of biological functions; it has been attracting increasing interest because of its potential applications in the biomedical field. The aim of this study was to develop a new sol-gel coating acting as a release vehicle of Mg, to enhance bioactivity of Ti materials and analyze the potential of this cation in bone regeneration.

The ^{29}Si-solid NMR showed that the incorporation of $MgCl_2$ into the sol-gel network did not affect the final silica network crosslinking. In addition, Mg ions did not form crystalline structures (as $MgCl_2$ precipitates), being were likely trapped on the hybrid structure through hydrogen bonding, Van der Waals or electrostatic

forces. Even though the Mg-doping did not change the material roughness, the contact angle significantly increased in comparison with the non-Mg coating regardless of the Mg concentration. Given that the roughness does not vary between compositions and that the degree of condensation of the synthetized networks is similar according to the chemical characterization, a possible explanation for the reduction observed in hydrophilicity could be associated with the presence of ions in the sol-gel structure and their effect in the Van der Waals and electrostatic forces [32]. As expected [20,24], the rate of hydrolytic degradation increased as more $MgCl_2$ was incorporated into the sol-gel network, and more Mg^{2+} was liberated. The release of this ion was stable until the end of the assay, reaching the values of 3 ppm in the material with the highest concentration of Mg (MT1.5Mg). None of the materials was cytotoxic to the MC3T3-E1 cells. Similarly, Romero-Gavilán *et al.* [33] and Martinez-Ibañez *et al*. [17] developed sol-gel coatings using MTMOS, TEOS and 3-glycidoxypropyltrimethoxysilane (GPTMS) that showed good bioactivity and biocompatibility. Yoshizawa *et al.* [34] have reported that the Mg ion is non-cytotoxic at concentrations as high as 10 mM, thus confirming that the levels of Mg in the sol-gel coatings studied here were within the safe range.

Osteoblast cell adhesion and growth are promoted by Mg as it interacts with integrins, well-known transmembrane receptors necessary for cell adhesion and stability [12]. Yan *et al*. [3] have shown that bone-marrow-derived stem cells (BMSCs) seeded onto the titania nanotube arrays containing Mg develop extended filopodia and thicker cell walls, thus benefiting cell adhesion. Similarly, the MT1Mg and MT1.5Mg sol-gel coatings led to wide-spreading MC3T3-E1 osteoblastic cells, with protruding lamellipodia and a significantly higher surface area compared to the cells cultured in the MT. Zreiqat *et al*. [8] have shown that Mg ions added to a bioceramic substrate increase the cell adhesion and the expression of β1-, α5β1- and α3β1-integrins in human bone-derived cells (HBDC). Likewise, we showed that the Mg-doped coatings increase the expression of the β1- and α5-integrin genes, depending on the cation concentration and exposure time, thus confirming the effects of the coatings on cell adhesion.

Cell differentiation is critical for new bone formation [35], and Mg-based biomaterials have proven effects on osteogenesis. Yan *et al*. [3] and Yoshizawa *et al.* [34] have shown that Mg-treated materials promote osteogenic differentiation in BMSCs. Gao *et al.* [35] have demonstrated an increase in ALP activity and osteogenic gene expression in MC3T3-E1 cells exposed to Mg-coated Ti6Al4V. Li *et al.* [36] evaluated the osteogenic properties of a nanoporous titanium coating with different concentrations of magnesium acetate, which was able to promote the adhesion, proliferation, and differentiation of bone marrow mesenchymal stem cells (BMSCs). Similarly, our Mg-doped sol-gel coatings increase the ALP activity on MT1.5Mg and TGF-β, OSX, and RUNX2 gene expression, thus indicating an augmented osteoblastic cell differentiation and proliferation, which are indicators of bone formation [37,38].

Chronic inflammation caused by implanted materials is associated with macrophages, which are the key players in the immune system [39]. They can assume two phenotypes: M1 and M2. The M1 macrophages are

involved in pro-inflammatory functions and the production of IL-1β, IL-12, and TNF-α. The M2 macrophages promote tissue healing and the production of IL-10 and TGF-β [40]. There are several reports of magnesium effect on inflammation [6,41] and the response to biomaterials [7,42–44] by the regulation of macrophage polarization [7]. In this study, culturing the cells on the Mg-doped sol-gel materials caused a significant decrease in TNF-α secretion. It also significantly promoted the expression of IL-4 and TGF-β genes and the secretion of TGF-β in MT1.5Mg. These results suggest that the Mg-doped materials modulate the macrophage polarization towards the M2 phenotype. Li *et al.* [7] have reported similar results in RAW 264.7 cells exposed to Mg-doped titanium. They have verified that these materials cause a significant decrease in the levels of pro-inflammatory markers (CCR7, TNF-α, IL-1β) and increase the abundance of anti-inflammatory markers (CD206, IL-4, IL-10).

The proteins from biological fluids spontaneously adsorbing onto the biomaterial surfaces play a major role in determining the interactions between implants and tissues. Understanding this phenomenon is essential to comprehend the cell responses and improve the design of biocompatible materials [13]. Here, the nLC-MS/MS analysis of the protein layer identified 22 proteins preferentially adsorbed onto the sol-gel coatings with Mg. Three proteins related to the complement system (CO9, C1QC, and CO3) and one associated with innate/adaptive immunological responses (SAMP) [43] were detected on these coatings. The complement system uses a large number of proteins that can induce an inflammatory response and opsonize pathogens [46]. However, this immunological response is controlled by numerous factors, which affect this cascade at its different stages. Among these are the plasma protease C1 inhibitor (IC1), vitronectin (VTNC), clusterin (CLUS) and complement factor H (CFAH) [45]. These four proteins were significantly more adsorbed onto the surfaces with Mg. The CLUS protein (8-fold increase in adsorption) prevents excessive inflammation through the regulation of complement activity and NF-κB pathway and reduces the apoptosis and oxidative stress [46,47]. IC1, a member of the serpin family of protease inhibitors, exerts an anti-inflammatory effect by regulating the complement system and interacting with extracellular matrices and cells [48]. Similarly, VTNC can moderate the intensity and duration of the inflammatory response to injury [49]. The CFAH protein is a critical regulator of the alternative complement pathway and has been directly associated with the maintenance of bone architecture. The balance in the interactions between osteoblasts and osteoclasts can be altered in the absence of CFAH, leading to a reduction in tissue quality [50]. Moreover, four apolipoproteins (APO2, APOA1, APOA4, and APOL1), known for their role in the metabolism of lipids and the inhibition of the complement system [51], were also preferentially adsorbed onto Mg-containing surfaces. The increased affinity of Mg-doped coatings to these immune-response regulatory proteins can explain the anti-inflammatory potential observed *in vitro*.

The interaction of the host tissue cells with the implant surface is the key process in the integration of implanted material, modulating tissue regeneration. Several proteins related to cell adhesion and tissue regeneration preferentially adhered to the Mg-doped coatings. This is consistent with the *in vitro* results, which showed an increase in the osteogenic potential and cell adhesion on these materials. Desmoglein-1

(DSG1) and desmoplakin (DESP), mediators of cell–cell adhesion, are transmembrane glycoprotein components of desmosomes [52] and preferentially adhere to the Mg-enriched coatings. Moreover, VTCN, also found on the Mg-doped coatings, is one of the many proteins that regulate cell adhesion and tissue remodeling through the interaction with integrins [53,54]. Rivera-Chacon *et al.* [55] have shown that the nanoporous TiO_2 templates that absorbed more VTNC boosted the osteoblast attachment and proliferation and, consequently, improve osteoconduction. Li *et al.* [56] have reported that the VTNC adsorption onto a biomaterial surface affects the spreading of human mesenchymal stem cells (hMSCs) and integrin expression. The increase in cell adhesion observed on the Mg-doped coatings is likely to be a result of the augmented gene expression of the integrins regulated by Mg. However, the increased abundance of VTNC on such surfaces and its subsequent interactions with these transmembrane receptors might also contribute to the overall effect. The impact of Mg-based biomaterials on cell adhesion have been associated with the stimulation of integrins [8]. However, the role of proteins adsorbed onto the biomaterials, as far as we know, has never been considered. Further studies are needed to better understand the manner in which the adsorbed proteins, such as VTNC, might affect the interaction between Mg and integrins, and thus promote the cell adhesion.

Among the proteins associated with tissue regeneration, cystatin-A (CYTA), also known as stefin A, belongs to a family of cysteine protease inhibitors and is coded by the *CSTA* gene. One of the functions of this protein is the inhibition of cathepsin B (CATB), H, and L. These lysosomal cysteine proteinases that can modulate the architecture of the extracellular matrix [57]. They are associated with several inflammatory diseases, including periodontitis [58–60]. Moreover, the VTCN regulates cascades related to other biological processes, such as coagulation and fibrinolysis. This is achieved through its interaction with heparin and thrombin–antithrombin III complexes [53]. Another protein associated with coagulation, alpha-2-macroglobulin (A2MG), also preferentially adsorbs to the Mg-doped coatings. This protein is an antiprotease that functions as an inhibitor of plasmin, kallikrein, and thrombin [61] and has important functions in the clearance of active proteases. Such proteases are important agents in connective tissue diseases and well-known virulence factors [62]. The A2MG has been suggested as a marker for the blood compatibility with a biomaterial as it is a sensitive marker for plasma protease activation on artificial surfaces [63].

These results show the potential of Mg in the development of biomaterials, revealing not only its overall effect on *in vitro* cell responses but also its role in the modulation of the protein adsorption patterns. It is possible to hypothesize that the well-known effects of magnesium biomaterials on cell adhesion, osteogenesis, and inflammation not only come from the properties of the ion itself, but also from the identified Mg-related proteins that attach to the surface upon implantation. With this, the results presented in this study shows a novel perspective of Mg in biomaterials as well as its effects on tissue regeneration.

5. Conclusion

The aim of this study was to further understand the effect of Mg on tissue regenerative processes. For that, we developed and characterized new Mg-enriched sol-gel coatings with a control release of the ion. The materials were successfully synthesized, with $MgCl_2$ well incorporated onto the sol-gel network, leading to a significant increase in the surface wettability in comparison with the base material. Unsurprisingly, the degradation increased with increasing Mg content, resulting in a steady release of Mg^{2+} until the end of the assay. The Mg-doped coatings preferentially adsorbed proteins related to inflammatory responses, cell adhesion, tissue regeneration, and coagulation. Concerning the inflammatory response, the reduction in TNF-α secretion and the increase in TGF-β and IL-4 gene expression indicate that the materials induced an anti-inflammatory phenotype. This was consistent with the increased adsorption of immune-system regulatory proteins (CLUS, CFAH, IC1 and VNTC). Moreover, the Mg-doped materials showed an increased affinity to the proteins related to cell adhesion (DESP, FILA2, and DSG1) and to the VTNC. This can explain the changes in the cell cytoskeleton arrangement with the consequent observed increase in the cell surface area. The Mg-doped materials also provoked an increase in the integrin gene expression (ITGA5 and ITGB1). In MC3T3-E1 osteoblastic cells, ALP activity was augmented in MT1.5Mg; this was accompanied by increased expression of TGF-β, OSX and RUNX2 genes. This preferential adsorption of proteins related to tissue regeneration (CYTA and VTNC) indicated the regenerative potential of these materials. The anti-inflammatory properties of these materials in combination with improved cell adhesion and the observed osteogenic responses demonstrate their potential for enhanced bone healing, being this effect more prominent at the highest concentrations.

Author Contributions

Andreia Cerqueira: Conceptualization, Formal analysis, Investigation, Writing - Original Draft, Writing - Review & Editing **Francisco Romero-Gavilán**: Conceptualization, Formal analysis, Investigation, Writing – Original Draft, Writing - Review & Editing **Iñaki García-Arnáez**: Methodology, Investigation **Cristina Martinez-Ramos:** Methodology, Resources **Seda Ozturan:** Methodology, Resources **R. Izquierdo:** Resources, Funding acquisition **Mikel Azkargorta:** Investigation, Data Curation **Félix Elortza:** Data Curation, Writing - Review & Editing **Mariló Gurruchaga:** Conceptualization, Writing - Review & Editing, Funding acquisition **Isabel Goñi:** Conceptualization, Writing - Review & Editing, Funding acquisition **Julio Suay:** Conceptualization, Writing - Review & Editing, Funding acquisition

Conflicts of interest

No conflicts of interest are reported.

Acknowledgements

This work was supported by MINECO [MAT2017-86043-R; RTC-2017-6147-1], Generalitat Valenciana [GRISOLIAP/2018/091, APOSTD/2020/036, PROMETEO/2020/069], Universitat Jaume I under [UJI-B2017-37, Posdoc/2019/28], the University of the Basque Country under [GIU18/189] and Basque Government under [PRE_2017_2_0044]. The authors would like to thank Raquel Oliver, Jose Ortega, José Miguel Pedra and Iraide Escobés for their valuable technical assistance and Antonio Coso (GMI-Ilerimplant) for producing the titanium discs.

References

1 E. O'Neill, G. Awale, L. Daneshmandi, O. Umerah and K. W. H. Lo, *Drug Discov. Today*, 2018, **23**, 879–890.

2 S. Castiglioni, A. Cazzaniga, W. Albisetti and J. Maier, *Nutrients*, 2013, **5**, 3022–3033.

3 Y. Yan, Y. Wei, R. Yang, L. Xia, C. Zhao, B. Gao, X. Zhang, J. Fu, Q. Wang and N. Xu, *Colloids Surfaces B Biointerfaces*, 2019, **179**, 309–316.

4 N. Nassif and I. Ghayad, *Adv. Mater. Sci. Eng.*, , DOI:10.1155/2013/532896.

5 M. M. Belluci, T. Schoenmaker, C. Rossa-Junior, S. R. Orrico, T. J. de Vries and V. Everts, *J. Nutr. Biochem.*, 2013, **24**, 1488–1498.

6 J. Sugimoto, A. M. Romani, A. M. Valentin-Torres, A. A. Luciano, C. M. Ramirez Kitchen, N. Funderburg, S. Mesiano and H. B. Bernstein, *J. Immunol.*, 2012, **188**, 6338–6346.

7 B. Li, H. Cao, Y. Zhao, M. Cheng, H. Qin, T. Cheng, Y. Hu, X. Zhang and X. Liu, *Sci. Rep.*, 2017, **7**, 42707.

8 H. Zreiqat, C. R. Howlett, a. Zannettino, P. Evans, G. Schulze-Tanzil, C. Knabe and M. Shakibaei, *J. Biomed. Mater. Res.*, 2002, **62**, 175–184.

9 H. Hornberger, S. Virtanen and A. R. Boccaccini, *Acta Biomater.*, 2012, 8, 2442–2455.

10 M. Diba, F. Tapia, A. R. Boccaccini and L. a. Strobel, *Int. J. Appl. Glas. Sci.*, 2012, **3**, 221–253.

11 S. fang Zhao, Q. hong Jiang, S. Peel, X. xiang Wang and F. ming He, *Clin. Oral Implants Res.*, 2013, **24**, 34–41.

12 Z. Wu, T. Tang, H. Guo, S. Tang, Y. Niu, J. Zhang, W. Zhang, R. Ma, J. Su, C. Liu and J. Wei,

Colloids Surfaces B Biointerfaces, 2014, **120**, 38–46.

13 S. Höhn, S. Virtanen and A. R. Boccaccini, *Appl. Surf. Sci.*, 2019, **464**, 212–219.

14 S. Galli, Y. Naito, J. Karlsson, W. He, I. Miyamoto, Y. Xue, M. Andersson, K. Mustafa, A. Wennerberg and R. Jimbo, *Acta Biomater.*, 2014, **10**, 5193–5201.

15 C. E. Wen, W. Xu, W. Y. Hu and P. D. Hodgson, *Acta Biomater.*, 2007, **3**, 403–410.

16 J. A. Oshiro, M. P. Abuçafy, E. B. Manaia, B. L. Da Silva, B. G. Chiari-Andréo and L. A. Chiavacci, *Polymers (Basel).*, , DOI:10.3390/polym8040091.

17 M. Martínez-Ibáñez, M. J. Juan-Díaz, I. Lara-Saez, A. Coso, J. Franco, M. Gurruchaga, J. Suay Antón and I. Goñi, *J. Mater. Sci. Mater. Med.*, , DOI:10.1007/s10856-016-5690-9.

18 N. Araújo-Gomes, F. Romero-Gavilán, I. García-Arnáez, C. Martínez-Ramos, A. M. Sánchez-Pérez, M. Azkargorta, F. Elortza, J. J. M. de Llano, M. Gurruchaga, I. Goñi and J. Suay, *J. Biol. Inorg. Chem.*, 2018, **23**, 459–470.

19 S. Oughlis, S. Lessim, S. Changotade, F. Bollotte, F. Poirier, G. Helary, J. J. Lataillade, V. Migonney and D. Lutomski, *J. Chromatogr. B Anal. Technol. Biomed. Life Sci.*, 2011, **879**, 3681–3687.

20 F. Romero-Gavilán, N. Araújo-Gomes, A. Cerqueira, I. García-Arnáez, C. Martínez-Ramos, M. Azkargorta, I. Iloro, M. Gurruchaga, J. Suay and I. Goñi, *JBIC J. Biol. Inorg. Chem.*, 2019, **24**, 563–574.

21 F. Romero-Gavilán, S. Barros-Silva, J. García-Cañadas, B. Palla, R. Izquierdo, M. Gurruchaga, I. Goñi and J. Suay, *J. Non. Cryst. Solids*, 2016, **453**, 66–73.

22 International Organization for Standardization, 2009, **3 ED**, 42.

23 International Organization for Standardization, .

24 A. Cerqueira, F. Romero-Gavilán, N. Araújo-Gomes, I. García-Arnáez, C. Martinez-Ramos, S. Ozturan, M. Azkargorta, F. Elortza, M. Gurruchaga, J. Suay and I. Goñi, *Mater. Sci. Eng. C*, 2020, **116**, 111262.

25 F. Romero-Gavilán, A. M. Sanchez-Pérez, N. Araújo-Gomes, M. Azkargorta, I. Iloro, F. Elortza, M. Gurruchaga, I. Goñi and J. Suay, *Biofouling*, 2017, **33**, 676–689.

26 F. Romero-Gavilán, J. Carlos-Almeida, A. Cerqueira, M. Gurruchaga, I. Goñi, I. M. Miranda-Salvado, M. H. Vaz Fernandes and J. Suay, *Prog. Org. Coatings*, 2020, **147**, 105770.

27 H. N. Kim and S. K. Lee, *Geochim. Cosmochim. Acta*, 2013, **120**, 39–64.

28 G. Chernev, N. Rangelova, P. Djambazki, S. Nenkova, I. Salvado, M. Fernandes, A. Wu and L. Kabaivanova, *J. Sol-Gel Sci. Technol.*, 2011, **58**, 619–624.

29 C. Gao, S. Peng, P. Feng and C. Shuai, *Bone Res.*, 2017, 5, 1–33.

30 F. Romero Gavilán, N. Araújo-Gomes, A. Cerqueira, I. Garcia Arnáez, C. Martínez Ramos, M. Azkargorta, I. Iloro, F. Elortza, M. Gurruchaga, J. Suay and I. Goñi, *JBIC J. Biol. Inorg. Chem.*, 2019, **24**, 563–574.

31 F. Romero-Gavilán, N. Araújo-Gomes, I. García-Arnáez, C. Martínez-Ramos, F. Elortza, M. Azkargorta, I. Iloro, M. Gurruchaga, J. Suay and I. Goñi, *Colloids Surfaces B Biointerfaces*, 2019, **174**, 9–16.

32 N. Novin, A. Shameli, E. Balali and S. Zomorodbakhsh, *J. Nanostructure Chem.*, 2020, **10**, 69–74.

33 F. Romero-Gavilan, N. Araújo-Gomes, A. M. Sánchez-Pérez, I. García-Arnáez, F. Elortza, M. Azkargorta, J. J. M. de Llano, C. Carda, M. Gurruchaga, J. Suay and I. Goñi, *Colloids Surfaces B Biointerfaces*, 2017, **162**, 316–325.

34 S. Yoshizawa, A. Brown, A. Barchowsk and C. Sfei, *Acta Biomater.*, 2014, **10**, 2834–2842.

35 P. Gao, B. Fan, X. Yu, W. Liu, J. Wu, L. Shi, D. Yang, L. Tan, P. Wan, Y. Hao, S. Li, W. Hou, K. Yang, X. Li and Z. Guo, *Bioact. Mater.*, 2020, **5**, 680–693.

36 X. Li, M. Wang, W. Zhang, Y. Bai, Y. Liu, J. Meng and L. Zhang, *Int. J. Nanomedicine*, 2020, **15**, 6593–6603.

37 K. Janssens, P. Ten Dijke, S. Janssens and W. Van Hul, *Endocr. Rev.*, 2005, 26, 743–774.

38 S. Wang, C. Xu, S. Yu, X. Wu, Z. Jie and H. Dai, *J. Mech. Behav. Biomed. Mater.*, 2019, **94**, 42–50.

39 R. M. Lozano, B. T. Pérez-Maceda, M. Carboneras, E. Onofre-Bustamante, M. C. García-Alonso and M. L. Escudero, *J. Biomed. Mater. Res. Part A*, 2013, **101**, 2753–2762.

40 Q. Gu, H. Yang and Q. Shi, *J. Orthop. Transl.*, 2017, **10**, 86–93.

41 A. Mazur, J. A. M. Maier, E. Rock, E. Gueux, W. Nowacki and Y. Rayssiguier, *Arch. Biochem. Biophys.*, 2007, **458**, 48–56.

42 S. C. Cifuentes, F. Bensiamar, A. M. Gallardo-Moreno, T. A. Osswald, J. L. González-Carrasco, R. Benavente, M. L. González-Martín, E. García-Rey, N. Vilaboa and L. Saldaña, *J. Biomed. Mater. Res. Part A*, 2016, **104**, 866–878.

43 Q. Peng, K. Li, Z. Han, E. Wang, Z. Xu, R. Liu and Y. Tian, *J. Biomed. Mater. Res. Part A*, 2013, **101A**, 1898–1906.

44 M. D. Costantino, A. Schuster, H. Helmholz, A. Meyer-Rachner, R. Willumeit-Römer and B. J. C. Luthringer-Feyerabend, *Acta Biomater.*, 2020, **101**, 598–608.

45 N. S. Merle, S. E. Church, V. Fremeaux-Bacchi and L. T. Roumenina, *Front. Immunol.*, 2015, **6**, 1–30.

46 Z. C. Wu, J. T. Yu, Y. Li and L. Tan, in *Advances in Clinical Chemistry*, Academic Press Inc., 2012, vol. 56, pp. 155–173.

47 G. Falgarone and G. Chiocchia, *Adv. Cancer Res.*, 2009, 104, 139–170.

48 A. E. Davis, P. Mejia and F. Lu, *Mol. Immunol.*, 2008, 45, 4057–4063.

49 D. I. Leavesley, A. S. Kashyap, T. Croll, M. Sivaramakrishnan, A. Shokoohmand, B. G. Hollier and Z. Upton, *IUBMB Life*, 2013, **65**, 807–818.

50 J. J. Alexander, J. S. Sankaran, K. L. Seldeen, R. Thiyagarajan, A. Jacob, R. J. Quigg, B. R. Troen and S. Judex, *Immunobiology*, 2018, **223**, 761–771.

51 N. H. Cho and S. Y. Seong, *Immunology*, 2009, **128**, 479–486.

52 J. L. Johnson, N. A. Najor and K. J. Green, *Cold Spring Harb. Perspect. Med.*, , DOI:10.1101/cshperspect.a015297.

53 S. Bierbaum, V. Hintze and D. Scharnweber, in *Comprehensive Biomaterials II*, Elsevier, 2017, pp. 147–178.

54 T. J. Rowland, L. M. Miller, A. J. Blaschke, E. L. Doss, A. J. Bonham, S. T. Hikita, L. V. Johnson and D. O. Clegg, *Stem Cells Dev.*, 2010, **19**, 1231–1240.

55 D. M. Rivera-Chacon, M. Alvarado-Velez, C. Y. Acevedo-Morantes, S. P. Singh, E. Gultepe, D. Nagesha, S. Sridhar and J. E. Ramirez-Vick, *J. Biomed. Nanotechnol.*, , DOI:10.1166/jbn.2013.1601.

56 T. Li, L. Hao, J. Li, C. Du and Y. Wang, *Bioact. Mater.*, 2020, **5**, 1044–1052.

57 S. M. Soond, M. V. Kozhevnikova, A. A. Zamyatnin and P. A. Townsend, *Pharmaceuticals*, 2019, 12.

58 X. Li, Z. Wu, J. Ni, Y. Liu, J. Meng, W. Yu, H. Nakanishi and Y. Zhou, *Oxid. Med. Cell. Longev.*, , DOI:10.1155/2016/7894247.

59 E. Ichimaru, M. Tanoue, M. Tani, Y. Tani, T. Kaneko, Y. Iwasaki, K. Kunimatsu and I. Kato, *Inflamm. Res.*, 1996, **45**, 277–282.

60 K. Kunimatsu, K. Yamamoto, E. Ichimaru, Y. Kato and I. Kato, *J. Periodontal Res.*, 1990, **25**, 69–73.

61 J. H. Cater, M. R. Wilson and A. R. Wyatt, *Oxid. Med. Cell. Longev.*, 2019, **2019**, 9.

62 P. B. Armstrong and J. P. Quigley, *Dev. Comp. Immunol.*, 1999, **23**, 375–390.

63 D. Biltoft, J. B. Gram, A. Larsen, A. M. B. Münster, J. J. Sidelmann, K. Skjoedt and Y. Palarasah, *Clin. Biochem.*, 2017, **50**, 1203–1208.

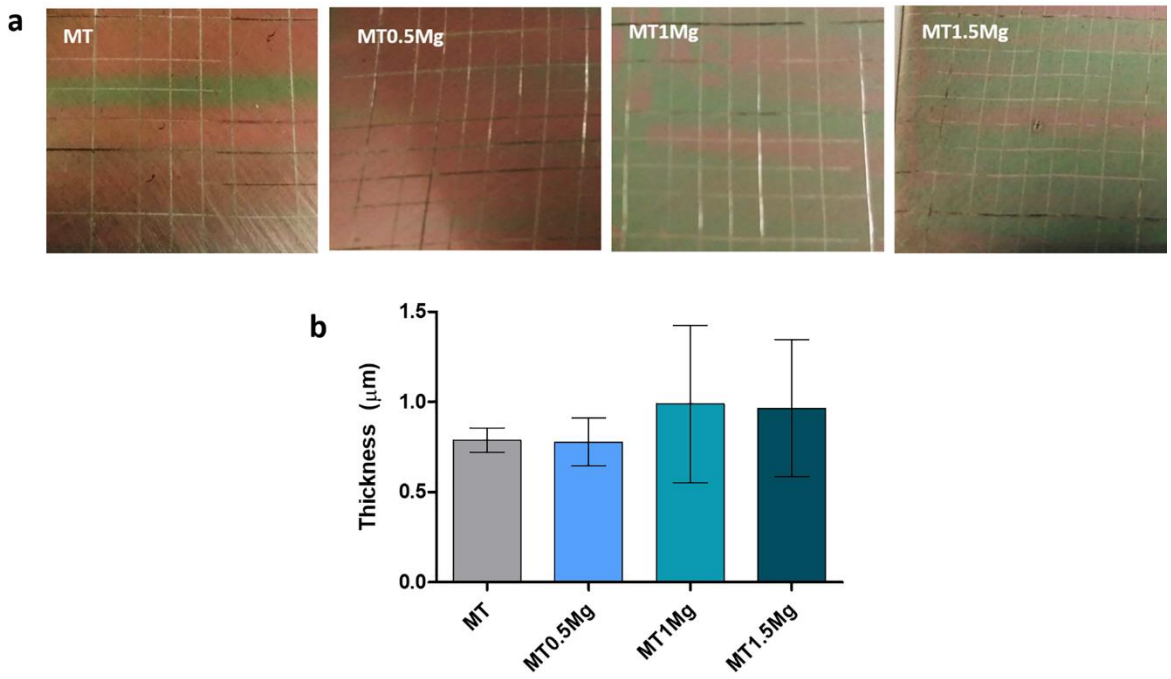

633

634 **Supplementary Figure 1.** Cross-cut test results (a) and thickness measurements (b). Results are
635 shown as means ± SE.

636